Miniature Flipping Disk Device for Size Measurement of Objects Through Endoscope

Wook Choi, Vladimir Rubtsov, and Chang-Jin "CJ" Kim, *Member, IEEE*

***Abstract*—Finding the size and distance of objects viewed through a single optical path—a typical endoscopic condition—is a challenge. Stereo imaging, which would provide the size and distance information, typically requires multiple optical channels or other elaborate techniques, increasing the endoscope diameter and system complexity. This paper reports the development of a miniature flipping disk device that enables stereo measurement, and demonstrates the operation of the device installed in an endoscope. The fabricated Pyrex disk (1.2 mm in diameter and 485 μm in thickness), anodically bonded to a 50-μm-thick silicon vertical comb-drive actuator, is flipped to $\pm 10.7^\circ$ at a resonant frequency of 414 Hz by 10 V_{AC} of electrostatic actuation. The image shift made by such glass flipping provides a reference dimension, against which the real size and distance of objects seen through a standard single-channel endoscope can be estimated. [2011-0320]**

***Index Terms*—Electrostatic actuation, endoscope, endoscopic observation, optical microelectromechanical systems (MEMS).**

I. Introduction

PROVIDING real-time images of difficult-to-access areas, today's endoscopy has become an indispensable tool for industrial and medical inspections [1]–[5]. Requiring only a small opening, endoscopic procedures have greatly reduced the cost and time for industrial inspection and prevented open surgeries for medical diagnoses and treatments. While widely practiced, however, one inconvenience of common endoscopic observations is that the images are generally planar with a large depth of focus, not providing the size and distance information of the viewed objects.

Such information can be obtained from stereo imaging through various triangulation techniques. Providing 3-D perception to the viewers in fields as diverse as medical [6], academic [7], and cinematic [8], most stereo imaging techniques use multiple optical setups to capture images of an object from different viewing angles [9], [10]. Although some endoscopes are indeed equipped with such multioptic systems [11], [12], an increase in structural complexity and overall diameter is inevitable.

Manuscript received October 31, 2011; revised March 12, 2012; accepted March 18, 2012. Date of publication May 8, 2012; date of current version July 27, 2012. This work was supported in part by the National Science Foundation Small Business Innovative Research program. Subject Editor A. J. Ricco.

W. Choi and C.-J. Kim are with the Department of Mechanical and Aerospace Engineering, University of California at Los Angeles, Los Angeles, CA 90095 USA (e-mail: cw0101@ucla.edu; cjkim@ucla.edu).

V. Rubtsov is with Intelligent Optical Systems, Inc. (IOS), Torrance, CA 90505 USA (e-mail: vrubtsov@intopsys.com).

Color versions of one or more of the figures in this paper are available online at http://ieeexplore.ieee.org.

Digital Object Identifier 10.1109/JMEMS.2012.2194774

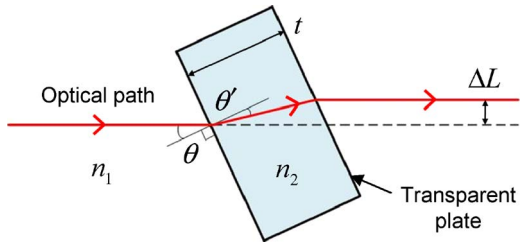

Fig. 1. Image shift by a transparent plate. A light ray is refracted as it passes through the tilted plate, shifting its optical path by ΔL. The amount of the shift is determined by the refractive indices of the media n_1 and n_2, as well as the tilted angle θ. This image shift by a tilted plate was used by Nishimoto and Shirai [16] to acquire separate images for stereo.

For many endoscopic applications where the tool diameter is of utmost importance, a measurement system that works with a single-optic endoscope would greatly increase the efficiency and accuracy of the inspection performance. We have considered various image separation methods that do not require additional optical channels [13]–[16], and introduced at a technical conference [17] a miniature flipping glass disk for size measurement under the microscope, based on the image separation method of Nishimoto and Shirai [16]. In this paper, we report a significantly improved (e.g., over three times larger flipping angle) device and its packaging in a custom-made endoscopic system equipped with imaging and illuminating components. Successful operation demonstrates how a microelectromechanical systems (MEMS) device can benefit visual inspectors by adding measurement capabilities to a conventional endoscope.

II. Concept: Size Estimation by a Flipping Disk

A. Image Shift by a Tilted Transparent Plate

The optical path of a light ray in one medium can be bent by having it pass through another medium. Such refraction of light is well explained by Snell's law, which relates the refractive indices of each medium n_1 and n_2, the incident angle θ of the light ray to the second medium, and the refracted angle θ' in the second medium. Fig. 1 shows the image-shifting method used in this paper by such refraction of light. When a flat and transparent plate is placed on the optical axis at an oblique angle, the light path shifts upward or downward, depending on the plate's tilting direction. The resulting shift (ΔL) can be calculated using the following equation [18]:

$$\Delta L = t \cdot \sin\theta \left[1 - \sqrt{\frac{1-\sin^2\theta}{\left(\frac{n_2}{n_1}\right)^2 - \sin^2\theta}}\right] \tag{1}$$

where t is the thickness of the plate.

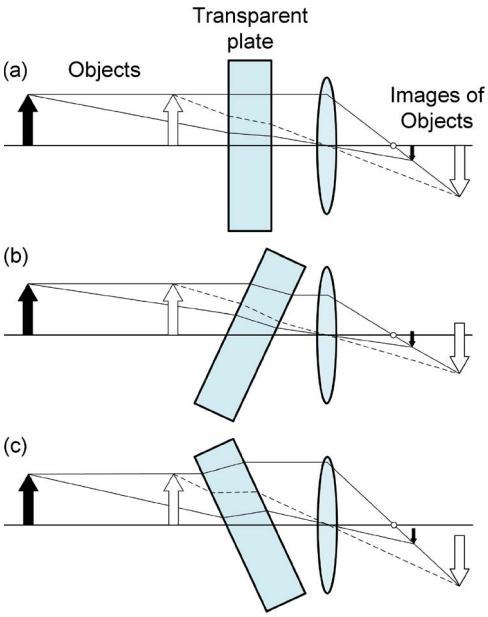

Fig. 2. Image shift by a transparent plate in front of an imaging system. (a) When the plate is normal to the optical path, the inverted images of the objects on optical axis stay on the optical axis. (b) When the plate rotates clockwise, the inverted images of the objects shift upward. (c) When the plate rotates counterclockwise, the images shift downward. In (b) and (c), the amounts of image shifts differ, depending on the objects' physical distances from the lens.

B. Size Estimation Using the Image Shift

Fig. 1 describes a situation when no lens is used in the optical axis, and the value found in (1) is the absolute image shift generated solely by the tilted plate, regardless of the distance to the object. If such a plate is used in front of an optical system (with lenses, e.g., eye, camera, or endoscope), the image shift ΔL is observed differently, depending on the object distances. Such distance-dependent observed shift can be used to determine the size of an object seen through the plate without knowing the actual distance to the object.

Fig. 2 shows how the amount of image shift depends on the distance to an object when the plate is flipped in front of an imaging system. When the plate is normal to the optical axis as in Fig. 2(a), the two objects (one closer to and one farther from the lens) on the optical axis make inverted images standing on the same optical axis. When the plate tilts clockwise [Fig. 2(b)] or counterclockwise [Fig. 2(c)], the images of the objects shift upward or downward, respectively, due to the refractions through the transparent plate. However, the amounts of shift are different, depending on each object's distance from the objective lens used in the imaging system. That is, the image of the closer object shifts more than that of the farther one. Regardless of the different shifting amounts for objects at different distances, note that all the imaging shifts represent the absolute image shift ΔL found in (1) at a specific tilting angle. Since ΔL is already known for a given plate tilting angle, the real object size can be found, regardless of distance, by comparing the observed object image size with the observed shift amount.

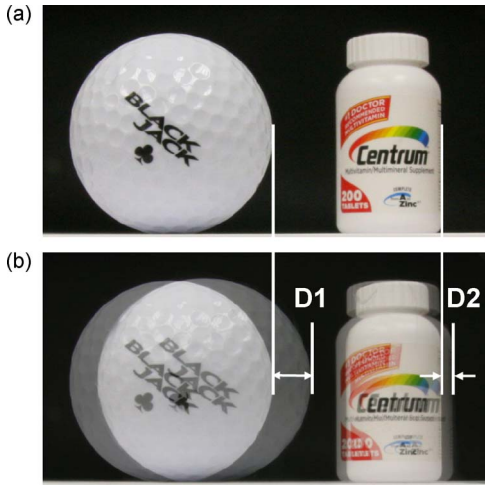

Fig. 3. Image-shifting experiment with a transparent plate placed in front of a camera. (a) Two objects are at different distances from the observer. Because the distance to each object is unknown, the real object sizes cannot be found. (b) When the plate is tilted, their images shift in different amounts (D1 and D2) based on their distances. The real sizes can be estimated using D1 and D2 as reference dimensions.

C. Simple Experiment

For example, Fig. 3(a) shows two objects of different sizes (a golf ball and a vitamin bottle) at unknown distances from the observer. Since the observer sees them through a single objective lens, the real size of each object cannot be found, unless an object of known dimension is available as a reference during the imaging. However, if a 2.1-cm-thick acrylic plate $(n = 1.49)$ is placed in front of the camera and tilted 60°, the images of those two objects show different shifting amounts (D1 and D2) as in Fig. 3(b)—the closer object shifts more. From (1), the absolute image shift by the given acrylic plate tilted 60° is found to be about 8 mm, which both D1 and D2 represent. By comparing D1 to the diameter of the ball image and D2 to the width of the bottle image, the size of each object can be found. Specifically, the diameter of the ball image is 5.3 times D1, which determines the diameter of the real ball to be 42.5 mm.

III. Design: Miniature Flipping Disk Device

A. Device Design and Operation

To realize the size estimation introduced in the previous section for endoscopic applications, a miniature device of a flipping disk is designed for MEMS fabrication. Fig. 4 shows the schematic of the miniature device, consisting of a glass disk, a silicon comb-drive actuator to flip the disk, and a glass ring structure to support the silicon actuator. The whole device is to be made into a thin cylindrical shape to fit in the endoscope that will be introduced in a later section.

Many of previously introduced optical MEMS devices [19]–[21] used photopatternable polymers (e.g., SU-8 or PDMS) as their lens material to keep the device fabrication simple. However, the use of such polymers invites many problems, such as stress mismatch, which warps the device, particularly if the substrate is thin, and poor adhesion to the substrate, as well as discoloration and degradation of the polymer during

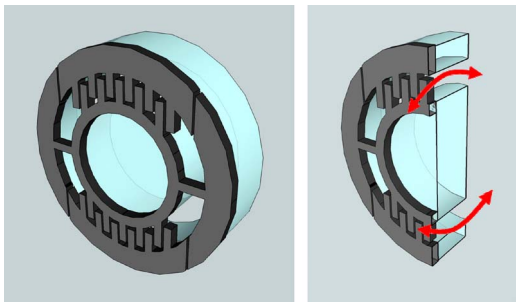

Fig. 4. Simplified schematic of the flipping disk device, consisting of a thin silicon layer anodically bonded on a glass layer. The glass disk is suspended by two silicon torsion bridges on both sides. The flipping motion is achieved by two sets of vertical (i.e., out-of-plane) comb drives patterned on the silicon layer bonded on the glass.

dry-etching processes or over time in use. To avoid these problems, we have chosen to use Pyrex (refractive index $n = 1.474$) for the transparent disk and bond it to a silicon actuator. To form the disk and the structural ring, we chose to use thermal molding [22] over isotropic wet etching [23] or other glass micromachining methods [24]–[26]. The molding allows glass structures to replicate the excellent vertical sidewalls of deep-reactive-ion-etching (DRIE)-processed silicon, solving the alignment problem between the glass structures and the silicon actuator. The vertical sidewall is important in order to fit the relatively thick glass structures in the limited cross-sectional area of endoscopes.

As shown in the design layout of Fig. 5 (top), the silicon actuator has a circular opening at the center, two torsion bridges (on the left and right of the opening), and two sets of interdigitated comb drives (above and below the opening). This comb drive induces out-of-plane motions (vertical to its plane), instead of the usual in-plane motions, when the driving signal is synchronized with the disk's torsional resonant frequency. The entire actuator is made of a single silicon layer to avoid the complexity and ill effects of additional silicon or metal layers, through which asymmetric electric potentials are applied for vertical actuations [27], [28]. Such flipping motions of planar structures, demonstrated by several authors [29]–[31], can be initiated by the fabrication-induced asymmetry [29] and maintained at the torsional resonance for vertical motion. One driving signal is provided to the device through three electrodes: one (①) for ground and two (② and ③) that share the driving signal. For such single-layered vertical comb-drive actuators, a square pulse, instead of a sinusoidal driving signal, has been reported to produce larger flipping angles [31].

Fig. 5 (bottom) shows a driving electric signal (solid line), the resultant flipping angle of the disk (dashed line), and the corresponding statuses of a resonating disk in cross sections. A driving pulse with a duty cycle of 50% is applied at twice the mechanical resonant frequency of the flipping disk. An electric potential is applied when the disk reaches the maximum flipping angle to rotate the disk in the other direction, and the potential is removed when the disk reaches the minimum angle (i.e., flat with the device surface) so that it continues rotating to the other maximum angle by inertia. That is, two periods of the driving signals are needed to complete the disk's one mechanical flipping cycle, requiring the driving signal to be

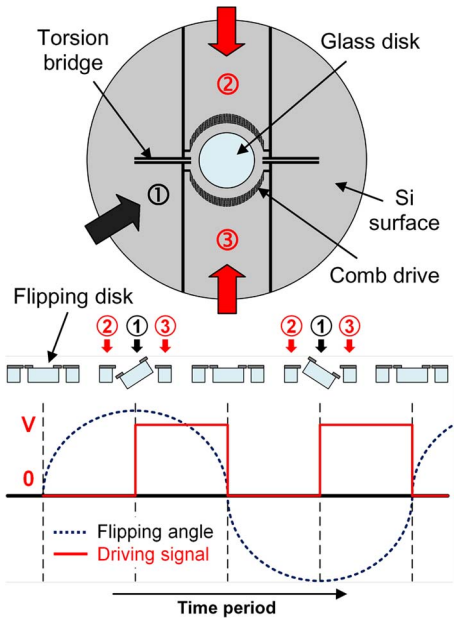

Fig. 5. Design layout for the disk-flipping silicon device, drawn reasonably to scale. (Top) The device consists of three electrode areas: ① for ground, and ② and ③ for actuating signal. ② and ③ share the same electric signal. (Bottom) A pulse signal (solid) is used to drive the flipping disk whose angle is represented by the dashed line. The driving signal has a duty cycle of 50% at twice the mechanical resonant frequency of the disk.

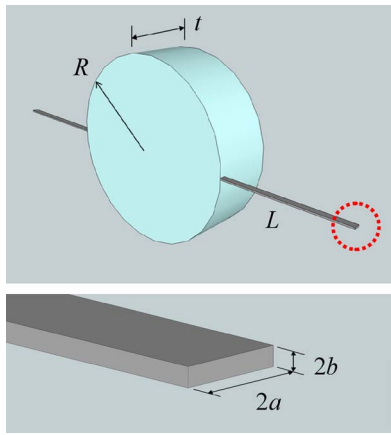

Fig. 6. Simplified view of the flipping disk device to calculate the torsional resonant frequency.

twice the mechanical resonant frequency of the disk. As the device operates, the imaging system located just behind the device captures the generated image shifts in synchronization with the flipping.

B. Torsional Resonant Frequency

To estimate the torsional resonant frequency of the disk, the flipping disk is vastly simplified as in Fig. 6, where two silicon bridges are attached to the disk. By using the dimensions of the silicon bridges, the torsional spring constant k_{Torsion} can be found using the following equations [32], [33]:

$$K \approx a \cdot b^3 \left[\frac{16}{3} - 3.36 \cdot \frac{b}{a} \cdot \left(1 - \frac{b^4}{12 \cdot a^4} \right) \right] \quad (a \geq b) \tag{2}$$

$$k_{\text{Torsion}} = \frac{K \cdot G}{L} \tag{3}$$

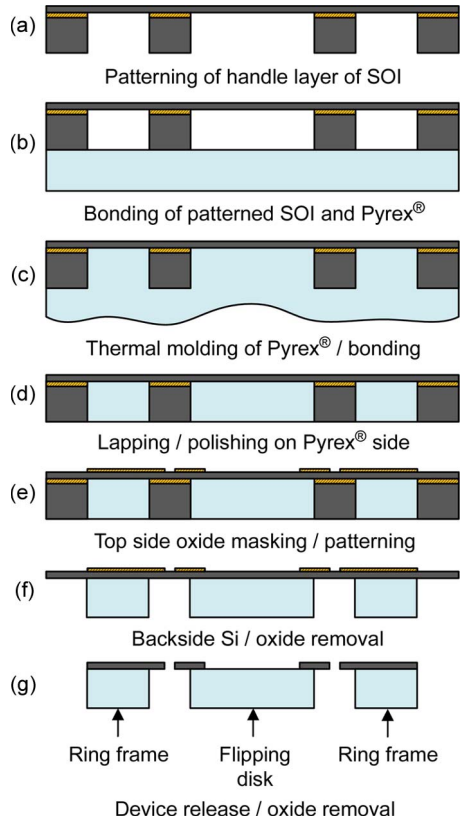

Fig. 7. Process sequence of the flipping disk device. (a) Preparation of silicon mold. (b–d) Formation of Pyrex disk and frame. (e–g) Patterning of silicon actuator and device release.

where

a half of the beam height;
b half the beam width;
K K factor of the beam;
G shear modulus of the beam material;
L length of each beam.

Using the spring constant k_{Torsion} found in (3), the mechanical resonant frequency f of the flipping device can be calculated by the following equations:

$$I_m = \frac{1}{4}m \cdot R^2 + \frac{1}{3}m \cdot t^2 \tag{4}$$

$$f = \frac{1}{2\pi}\sqrt{\frac{k_{\text{Torsion}}}{I_m}} \tag{5}$$

where

m mass of the disk;
R radius of the disk;
t thickness of the disk.

IV. Fabrication

A. Microfabrication of Device

The fabrication process of the flipping disk device largely consists of three steps: mold formation using a silicon-on-insulator (SOI) wafer, thermal glass reflow, and definition of the actuator. The main processing steps are described in Fig. 7. An SOI wafer with 50-μm Si device layer, 0.5-μm buried oxide, and 500-μm Si handle layer is used as the starting material. To eliminate the need for any metal layers deposited and patterned for electrode formation, an SOI wafer with a heavily doped device layer is selected. As the first step, the handle layer is etched by DRIE, and the exposed buried oxide is removed by hydrofluoric acid [Fig. 7(a)], forming a 500-μm-deep mold for glass structures. The patterned handle layer is then anodically bonded to a 1-mm-thick Pyrex wafer at 1200 V and 400 °C in a vacuum chamber kept under 1.2 Pa [Fig. 7(b)] to ensure that the cavities between the silicon and the glass wafer are free of gas.

The bonded wafers are heated at an elevated temperature ($\sim$750 °C: well above the glass transition temperature of Pyrex) in a furnace at atmospheric pressure to reflow the Pyrex into the silicon mold [22] for 3 h [Fig. 7(c)], followed by additional anodic bonding to strengthen the adhesion between the Pyrex and the silicon device layer. Because the molded glass is already in contact with the SOI's device layer, the use of vacuum for this anodic bonding is optional. The pressure difference between inside (vacuum) and outside (atmospheric) of the cavities drives Pyrex to automatically fill into the mold at the set temperature. The unfilled Pyrex material is then lapped away, followed by an additional polishing step to make the molded glass surfaces smooth for high transparency [Fig. 7(d)].

The next step is to pattern actuators for the device. A 3000-Å-thick silicon dioxide is deposited by plasma-enhanced chemical vapor deposition and patterned on the top of the Si device layer [Fig. 7(e)], which will later be used as a mask for final etching. All the silicon material in the handle layer is then removed by DRIE or wet silicon etching, and the exposed buried oxide is removed by RIE [Fig. 7(f)]. As a result of this step, only the molded glass structures are left under the Si device layer of the SOI. The final step is to pattern the Si device layer by DRIE to open the optical window for the Pyrex disk and form the comb-drive actuator, releasing the device at the same time [Fig. 7(g)].

Fig. 8 shows the backside photographs of the sample during the glass flowing, as molding steps progress. Fig. 8(a) is the mold before the thermal molding process started [equivalent to Fig. 7(a)]. Fig. 8(b) shows the Pyrex-filled SOI wafer after the thermal reflow [equivalent to Fig. 7(c)], and Fig. 8(c) is the sample with all the unfilled Pyrex lapped away [equivalent to Fig. 7(d)]. Fig. 8(d) shows the final glass structures [equivalent to Fig. 7(f)] that are 485 μm in thickness: a flipping disk at the center, a ring frame to support the top Si device layer, and the outermost protective structure used during the fabrication, which also bears alignment marks. During this process, about 30 μm of misalignment was observed between the silicon and the Pyrex, which did not have any noticeable effect on device operation.

A completed flipping disk device is shown in Fig. 9 (top) [equivalent to Fig. 7(g)]. The overall diameter of the device is 5 mm, and the central window opened for the underlying Pyrex disk is 1 mm in diameter. The Pyrex disk that is 1.2 mm in diameter and 485 μm in thickness is suspended by two 1000 μm (long) $\times$ 10 μm (wide) $\times$ 50 μm (thick) silicon torsion bridges. Because the electrostatic force pulls the tilted disk back to the flat position and keeps the device resonating

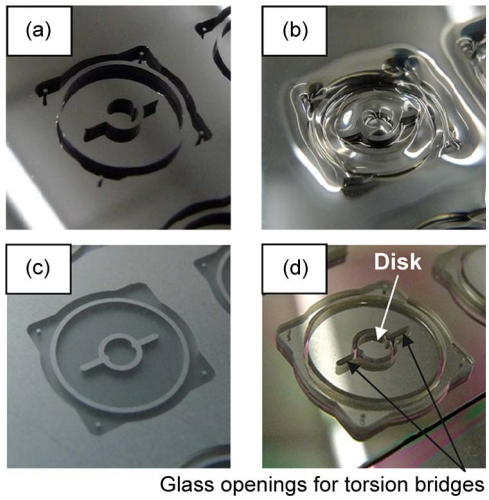

Fig. 8. Optical photographs during the glass structure formation, viewed from the backside of the sample. (a) A completed mold. (b) Pyrex is filled into the mold. (c) The excessive Pyrex is lapped away. (d) Silicon mold is removed. The disk is located in the center between the glass openings for torsion bridges.

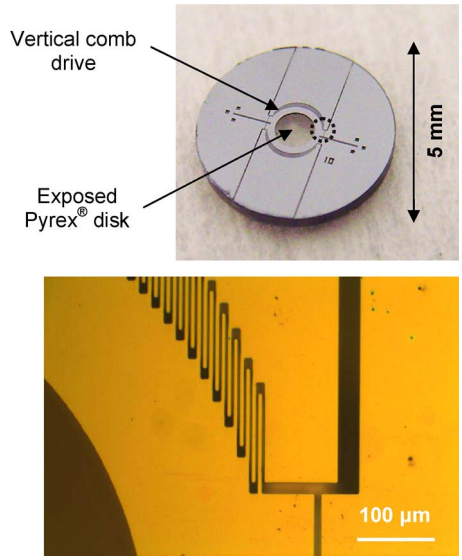

Fig. 9. Fabricated flipping disk device. (Top) The device is 5 mm in overall diameter and has a circular window opened at the center to expose the underlying Pyrex disk. (Bottom) The magnified photograph of the dotted circled area of (top), showing the patterned comb-drive structure.

as previously shown in Fig. 5, more comb fingers increase the rotating force and lower the driving voltage. For this reason, as many comb fingers were patterned in the device as allowed by the fabrication. Each of the two comb-drive actuators has 157 opposing fingers patterned on the Si device layer of the SOI wafer. Each finger is 130 μm long, 4 μm wide, and 50 μm thick, with 4-μm gap between the fingers, as shown in the microscopic image of Fig. 9 (bottom), where silicon is shown in light color and the gap in dark.

B. Device Packaging With Endoscope

For the eventual applications of inspecting hard-to-reach areas, the flipping disk device should operate as a part of endoscope systems. To demonstrate and characterize the flipping disk device with an endoscope, we have packaged the miniature device with a custom-manufactured endoscope system and

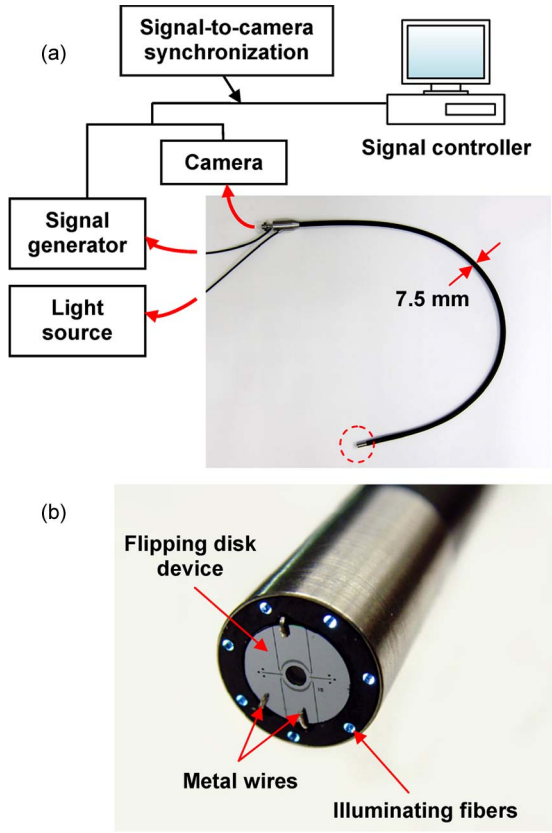

Fig. 10. Endoscope system manufactured for this paper. (a) Overall system configuration of the endoscope for both the flipper operation and image shift detection. The dotted circle indicates the distal end. (b) Photograph of the distal end. The flipper is inserted in the endoscope and electrically connected to the three metal wires. Around the flipper are the illuminating fibers to light up the work area.

performed stationary imaging tests on an optical table. The system consists of (1) the 60-cm-long endoscope with required optical circuit (custom-developed by OMEX Technologies, IL) connected to a charge-coupled device (CCD) camera (model # GX1660C, Allied Vision Technologies, MA) to transfer the acquired images, (2) the optical fiber-based illumination system connected to a light source (model # Q5000, Stryker, CA), (3) a handheld electric pulse signal generator, which drives the flipping device and synchronizes the signal with the CCD camera, and (4) the LabVIEW software to control the signal (frequency and amplitude) and resolve the acquired image shifts, as shown in Fig. 10 (top). The imaging software was designed based on the calculated resonant frequency of the flipping disk to capture images at the right moments when the disk is at the maximum angles. The endoscope is 7.5 mm in diameter and accommodates the fabricated device at the tip, as shown in Fig. 10 (bottom). The flipping disk device is plugged into a recess prepared in the endoscope and held by three metal wires bent into shape that also send the electric signals to the heavily doped silicon device from the signal generator connected at the other end. To ensure good electrical connection, silver paint is pasted around the contact points. Around the device are seven illuminating fibers to light up the work area.

The camera is synchronized to the driving electric signal and triggered at the pulse rising points to capture images when the Pyrex disk is at the maximum tilting positions, as shown in

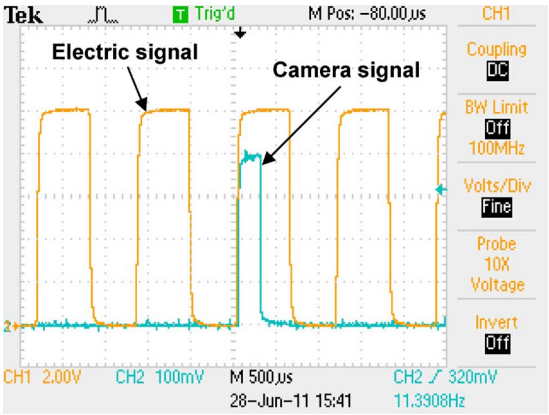

Fig. 11. Synchronized driving signal and the camera triggering signal to capture images at the maximum disk tilting. The camera is triggered at the rising points of the signal pulses.

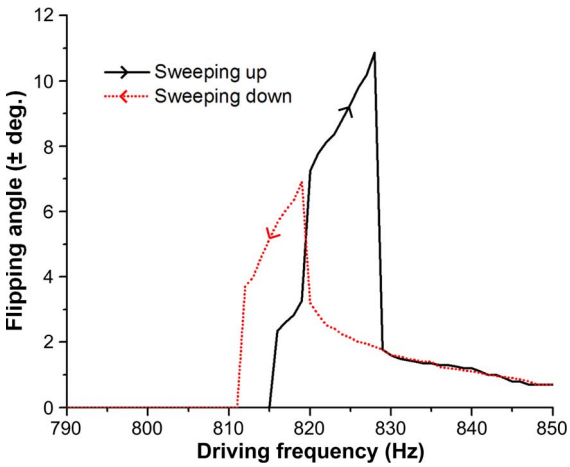

Fig. 12. Dynamic characterization of the flipping disk by frequency sweeping. Up to $\pm 10.7^\circ$ of flipping (21.4° in total) was obtained at 414 Hz, using 10 V_{AC} of pulse wave with 50% duty cycle at 828 Hz.

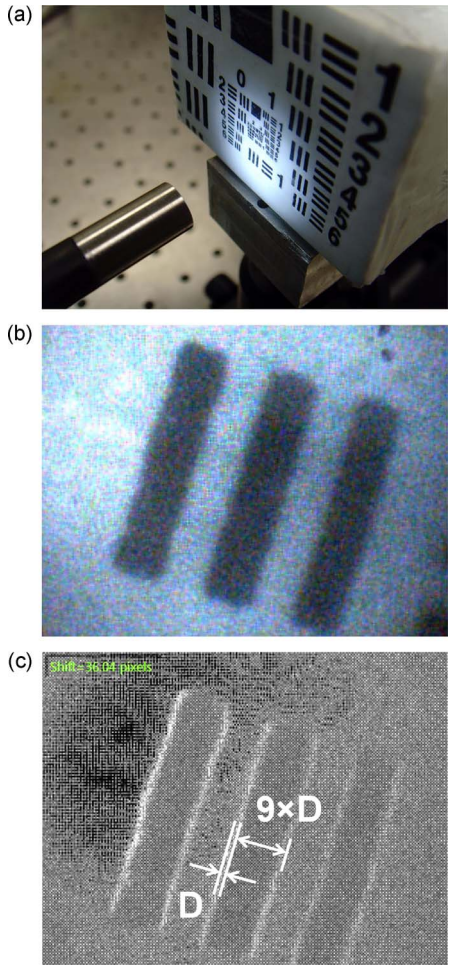

Fig. 13. Operation of the endoscope equipped with the flipping disk device. (a) The endoscope is pointing at an optical target (at an unknown distance) featuring line patterns (of unknown dimensions). (b) Captured line images when the disk flips to one extreme position. (c) Processed image using a set of two captured images at the two extreme disk angles. Width of the white line ("D") represents the amount of image shift generated by the disk flipping. D is used as a reference for size estimation of target objects.

Fig. 11. Even though the camera is programmed to be triggered at less than the camera's refresh rate of 62 Hz, which is lower than the disk's flipping frequencies, it captures the images at the right moments via this synchronization process.

V. Testing

A. Device Operation and Characterization

A square wave between 0 and 10 V is applied to the flipping disk device through the endoscope. The driving frequency is increased by 0.5-Hz increments until the disk resonates. Fig. 12 shows an experimental result showing the dynamic response of the disk as the frequency sweeps up and down while the flipping disk device is held vertically in the endoscope in an open lab environment. The disk begins resonating with 816-Hz driving frequency and reaches the maximum flipping angles of $\pm 10.7^\circ$ at 414 Hz with 828-Hz driving frequency. As the frequency is swept down, the disk meets a resonance with $\pm 6.7^\circ$ at 819-Hz driving frequency before the angle reduces. This test result is in good agreement with the theoretical resonance calculated for the given disk structure: 418 Hz.

B. System Operation to Demonstrate Measurements

Images are captured at the two extreme angles as the disk flips at 414 Hz (i.e., resonance). The images at each extreme are combined into one, and the two combined images undergo a real-time subtraction process to reveal the relative shift. The shift is shown as white lines, whose width represents the shifting amount. For image capturing, a printed optical target with various line patterns, shown in Fig. 13(a), is placed an unknown distance away from the device. The target is lit by the built-in illumination system of the endoscope setup.

Fig. 13(b) is a captured image at one extreme angle of the disk, showing the line patterns used as a target with unknown dimensions. Fig. 13(c) is the processed image with apparent image shift shown as white lines, using the imaging process described earlier. In order to increase the brightness and make the image shift more apparent, 50 of the same images are

superimposed. Using (1), the absolute image shift generated by the $\pm 10.7^\circ$ of disk flipping is found to be 59.1 μm. Setting the width of the white line as "D" (equivalent to 52.9 μm after compensating for the line broadening during the 250-μs exposure) as a reference, the width of the lines on the optical target can be estimated, regardless of the distance to the target. Measured to be approximately 9 times D, the linewidth is estimated to be about 476 μm, which is smaller than the real linewidth (500 μm) measured directly on the target. This deviation is likely from the errors in the shift measurement and the line-broadening compensation, which can be addressed if stronger illumination and shorter exposure time are used.

VI. Conclusion

We have developed an endoscope with a miniature flipping Pyrex disk. This paper has introduced the concept of size measurement with a flipping disk, has described the design and fabrication of the miniature flipping disk device, and has reported packaging of the device with a custom-manufactured endoscope. The micromolded Pyrex disk flipped to a total angle of 21.4° with a 10-V pulse signal, generating an image shift to be used as a reference for size estimation of objects at unknown distances. The completed endoscope was operated on a lab bench to confirm the size measurement. In a demonstration, 500-μm-wide printed lines were estimated to be approximately 476 μm. For the reported endoscope to function in real-life applications, the flipping disk at the end of the endoscope will need a transparent cap to avoid physical contact with the environment.

Acknowledgment

The authors would like to thank M. Levin for his help on the imaging test and experiment setup, M. Akbarian for her early assistance on optics, and J. Jenkins for the valuable discussions about the visualization and composition of the manuscript. The portable signal generator and the software program to visualize the line shift were developed by Dr. A. Berger.

References

[1] S. J. Spaner and G. L. Warnock, "A brief history of endoscopy, laparoscopy, and laparoscopic surgery," *J. Laparoendosc. Adv. Surg. Techn. A*, vol. 7, no. 6, pp. 369–373, Dec. 1997.

[2] G. Berci and K. A. Forde, "History of endoscopy: What lessons have we learned from the past?" *Surg. Endosc.*, vol. 14, no. 1, pp. 5–15, Jan. 2000.

[3] G. S. Litynski, "Endoscopic surgery: The history, the pioneers," *World J. Surg.*, vol. 23, no. 8, pp. 745–753, Aug. 1999.

[4] R. A. Miller, "Endoscopic instrumentation: Evolution, physical principles and clinical aspects," *Brit. Med. Bull.*, vol. 42, no. 3, pp. 223–225, Jul. 1986.

[5] K. B. Allen, G. L. Griffith, D. A. Heimansohn, R. J. Robison, R. G. Matheny, J. J. Schier, E. B. Fitzgerald, and C. J. Shaar, "Endoscopic versus traditional saphenous vein harvesting: A prospective, randomized trial," *Ann. Thoracic Surg.*, vol. 66, no. 1, pp. 26–31, Jul. 1998.

[6] A. F. Durrani and G. M. Preminger, "Three-dimensional video imaging for endoscopic surgery," *Comput. Biol. Med.*, vol. 25, no. 2, pp. 237–247, Mar. 1995.

[7] H. W. Schreier, D. Garcia, and M. A. Sutton, "Advances in light microscope stereo vision," *Exp. Mech.*, vol. 44, no. 3, pp. 278–288, Jun. 2004.

[8] L. Lipton, "Foundations of the Stereoscopic Cinema," New York: Van Nostrand Reinhold, 1982.

[9] G. A. Triantafyllidis, D. Tzovaras, and M. G. Strintzis, "Occlusion and visible background and foreground areas in stereo: A Bayesian approach," *IEEE Trans. Circuits Syst. Video Technol.*, vol. 10, no. 4, pp. 563–575, Jun. 2000.

[10] J. F. Cardenas-Garcia, H. G. Yao, and S. Zheng, "3D reconstruction of objects using stereo imaging," *Opt. Lasers Eng.*, vol. 22, no. 3, pp. 193–213, 1995.

[11] Example of stereo inspection systems found and accessed on 14 Jul 2011. [Online]. Available: http://www.olympus-ims.com/en/rvi-products/iplex-lx/#06

[12] H. Mayer, I. Nagy, A. Knoll, E. U. Braun, R. Bauernschmitt, and R. Lange, "Haptic feedback in a telepresence system for endoscopic heart surgery," *Presence, Teleoper. Virtual Environ.*, vol. 16, no. 5, pp. 459–470, Oct. 2007.

[13] A. Goshtasby and W. A. Gruver, "Design of a single-lens stereo camera system," *Pattern Recognit.*, vol. 26, no. 6, pp. 923–937, Jun. 1993.

[14] C. Gao and N. Ahuja, "Single camera stereo using planar parallel plate," in *Proc. Int. Conf. Pattern Recognit.*, 2004, vol. 4, pp. 108–111.

[15] D. H. Lee and I. S. Kweon, "A novel stereo camera system by a biprism," *IEEE Trans. Robot. Autom.*, vol. 16, no. 5, pp. 528–541, Oct. 2000.

[16] Y. Nishimoto and Y. Shirai, "A feature-based stereo model using small disparities," in *Proc. IEEE Int. Workshop Ind. Appl. Mach. Vis. Mach. Intell.—Seiken Symp.*, Tokyo, Japan, Feb. 1987, pp. 192–196.

[17] W. Choi, M. Akbarian, V. Rubtsov, and C.-J. Kim, "Microfabricated flipping glass disc for stereo imaging in endoscopic visual inspection," in *Proc. IEEE Int. Conf. MEMS*, Sorrento, Italy, Jan. 2009, pp. 160–163.

[18] W. J. Smith, *Modern Optical Engineering*. New York: McGraw-Hill, 2000.

[19] R. Yang and W. J. Wang, "Out-of-plane polymer refractive microlens fabricated based on direct lithography of SU-8," *Sens. Actuators A, Phys.*, vol. 113, no. 1, pp. 71–77, Jun. 2004.

[20] S. Camou, H. Fujita, and T. Fujii, "PDMS 2-D optical lens integrated with microfluidic channels: Principle and characterization," *Lab Chip*, vol. 3, no. 1, pp. 40–45, 2003.

[21] S. D. Moon, N. Lee, and S. Kang, "Fabrication of a microlens array using micro-compression molding with an electroformed mold insert," *J. Micromech. Microeng.*, vol. 13, no. 1, pp. 98–103, Jan. 2003.

[22] P. Merz, H. J. Quenzer, H. Bernt, B. Wagner, and M. Zoberbier, "A novel micromachining technology for structuring borosilicate glass substrates," in *Proc. TRANSDUCERS*, 2003, vol. 1, pp. 258–261.

[23] M. Q. Bu, T. Melvin, G. J. Ensell, J. S. Wilkinson, and A. G. R. Evans, "A new masking technology for deep glass etching and its microfluidic application," *Sens. Actuators A, Phys.*, vol. 115, no. 2/3, pp. 476–482, Sep. 2004.

[24] Z. Y. Yu, K. P. Rajurkar, and A. Tandon, "Study of 3D micro-ultrasonic machining," *J. Manuf. Sci. Eng.*, vol. 126, no. 4, pp. 727–732, Nov. 2004.

[25] S. Nikumb, Q. Chen, C. Li, H. Reshef, H. Y. Zheng, H. Qiu, and D. Low, "Precision glass machining, drilling and profile cutting by short pulse lasers," *Thin Solid Films*, vol. 477, no. 1/2, pp. 216–221, Apr. 2005.

[26] J. H. Park, N. E. Lee, J. Lee, J. S. Park, and H. D. Park, "Deep dry etching of borosilicate glass using SF6 and SF6/Ar inductively coupled plasmas," *Microelectron. Eng.*, vol. 82, no. 2, pp. 119–128, Oct. 2005.

[27] D. Hah, S. T. Y. Huang, J. C. Tsai, H. Toshiyoshi, and M. C. Wu, "Low-voltage, large-scan angle MEMS analog micromirror arrays with hidden vertical comb-drive actuators," *J. Microelectromech. Syst.*, vol. 13, no. 2, pp. 279–289, Apr. 2004.

[28] S. Kwon, V. Milanovic, and L. P. Lee, "Large-displacement vertical microlens scanner with low driving voltage," *IEEE Photon. Technol. Lett.*, vol. 14, no. 11, pp. 1572–1574, Nov. 2002.

[29] H. Schenk, P. Durr, T. Haase, D. Kunze, U. Sobe, H. Lakner, and H. Kuck, "Large deflection micromechanical scanning mirrors for linear scans and pattern generation," *IEEE J. Sel. Topics Quantum Electron.*, vol. 6, no. 5, pp. 715–722, Sep./Oct. 2000.

[30] K. N. Lee, Y. H. Jang, H. Kim, Y. S. Lee, and Y. K. Kim, "Monolithic fabrication of optical benches and scanning mirror using silicon micromachining," *J. Micromech. Microeng.*, vol. 15, no. 4, pp. 747–755, Apr. 2005.

[31] C. Lee, "Design and fabrication of epitaxial silicon micromirror devices," *Sens. Actuators A, Phys.*, vol. 115, no. 2/3, pp. 581–590, Sep. 2004.

[32] H. Urey, "Torsional MEMS scanner design for high resolution display systems," in *Proc. SPIE*, Seattle, WA, Jul. 2002, vol. 4773, pp. 27–37.

[33] W. Young and R. Budynas, *Roark's Formulas for Stress and Strain*. New York: McGraw-Hill, 2002.

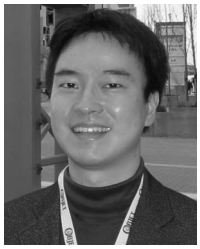

Wook Choi received the B.S. degree from the Mechanical Engineering Department, Kyungpook National University, Daegu, Korea, in 2002, and the M.S. and Ph.D. degrees from the Mechanical and Aerospace Engineering Department, University of California, Los Angeles (UCLA), in 2005 and 2011, respectively.

He is currently a Postdoctoral Researcher with the UCLA Micro and Nano Manufacturing Laboratory. His research interests include design and fabrication of pneumatic and electrostatic microdevices for various endoscopic applications using MEMS technologies.

Dr. Choi is currently a member of the Korean–American Scientists and Engineers Association (KSEA) and was a recipient of scholarships from the Korea Science and Engineering Foundation (KOSEF).

Vladimir Rubtsov received the Ph.D. degree in applied physics from the Nondestructive Control Research Institute, Kharkov, Ukraine (formerly U.S.S.R.).

His research career in the U.S. includes positions such as Staff Researcher with the Surgery Department Research Laboratory, UCLA Medical Center (Los Angeles, CA, 1992–2001), and Fiber Optic Program Manager with FarLight Corporation (Torrance, CA, 1996–2000). He joined Intelligent Optical Systems, Inc. (IOS), Torrance, as a Senior Scientist in 2000. His expertise is in nondestructive testing, fiber-optic and LED illumination, endoscopy, optical sensors, and fiber laser development. He has developed devices for the U.S. Navy, the U.S. Army, the National Institutes of Health, the National Science Foundation, the Defense Advanced Research Projects Agency, the U.S. Department of Homeland Security, and the National Aeronautics and Space Administration. He has conducted more than 50 projects and is a holder of four U.S. patents and seven Russian patents.

Chang-Jin "CJ" Kim (S'89–M'91) received the B.S. degree in mechanical engineering from Seoul National University, Seoul, Korea, the M.S. degree in mechanical engineering from Iowa State University, Ames, and the Ph.D. degree in mechanical engineering from the University of California at Berkeley, in 1991.

Since joining the faculty at the University of California at Los Angeles (UCLA), in 1993, he has developed several courses in microelectromechanical systems (MEMS) and established a MEMS Ph.D. major field in the Mechanical and Aerospace Engineering Department in 1997. Directing the Micro and Nano Manufacturing Laboratory, he is also a Founding Member of the California NanoSystems Institute (CNSI), UCLA. His research interests are in MEMS and nanotechnology, including design and fabrication of micro-/nanostructures, actuators, and systems, with a focus on the use of surface tension.

Dr. Kim has served on numerous technical committees and panels, including Transducers, the IEEE International Conference on MEMS, and the National Academies Panel on Benchmarking the Research Competitiveness of the U.S. in Mechanical Engineering. He is currently serving on the Editorial Advisory Board for the *IEEJ Transactions on Electrical and Electronic Engineering* and the Editorial Board for the JOURNAL OF MICROELECTROMECHANICAL SYSTEMS. A Fellow of the American Society of Mechanical Engineers, he was the recipient of the Graduate Research Excellence Award from Iowa State University, the 1995 TRW Outstanding Young Teacher Award, a 1997 NSF CAREER Award, the 2002 ALA Achievement Award, and the 2008 Samueli Outstanding Teaching Award. He has also been active in the commercial sector as a Board Member, Scientific Advisor, Consultant, and Founder of start-up companies.